

# Buckling of aboveground oil storage tanks under internal pressure

Shoichi Yoshida†

*Formerly Koyo Iron Works & Construction Company Tokyo, Japan*

**Abstract.** Overpressurization can occur due to the ignition of flammable vapors existing inside aboveground oil storage tanks. Such accidents could happen more frequently than other types of accident. In the tank design, when the internal pressure increases, the sidewall-to-roof joint is expected to fail before failure occurs in the sidewall-to-bottom joint. This design concept is the so-called “frangible roof joint” introduced in API Standard 650. The major failure mode is bifurcation buckling in this case. This paper presents the bifurcation buckling pressures in both joints under internal pressure. Elastic and elastic-plastic axisymmetric shell finite element analysis was performed involving large deformation in the prebuckling state. Results show that API Standard 650 does not evaluate the frangible roof joint design conservatively in small diameter tanks.

**Key words:** finite element method; axisymmetric shell; structural analysis; bifurcation buckling; elastic-plastic problem; large deformation; oil storage tank; internal pressure; frangible roof design.

---

## 1. Introduction

Aboveground oil storage tanks can be divided into two basic types as shown in Fig. 1:

fixed roof tanks and floating roof tanks. Fixed roof tanks are the subject of this paper and are usually used for small capacity storage. One type of accident with fixed roof tanks is overpressurization, which can occur due to the ignition of flammable vapors existing inside the tank. Overpressurization has occurred more frequently than other types of accident.

When the internal pressure exceeds the capability of the pressure relief vents attached to the fixed roof, the tank may fail. There are two failure types: the failure of the sidewall-to-bottom joint and that of the sidewall-to-roof joint, as shown in Fig. 2(a) and (b). The former can result in spillage of the tank’s contents and fire outside the tank. For this reason, it is much better for failure to occur in the sidewall-to-roof joint before the sidewall-to-bottom joint during overpressurization. This concept was introduced into a design rule in the API (American Petroleum Institute) standard 650, Appendix F as a “frangible roof joint” (Lu *et al.* 1996). However, experience has shown that the rule does not always perform as intended, especially for small diameter tanks (Morgenegg 1978).

When the tank is subjected to internal pressure, the sidewall-to-bottom joint is uplifted, and both the sidewall-to-bottom joint and the sidewall-to-roof joint deform greatly as they are pulled radially inward and compressed circumferentially as illustrated in Fig. 2(c). Stresses in both joints could exceed the material’s yield stress. As a result, this pressure could cause bifurcation buckling with a high

---

†Ph.D.

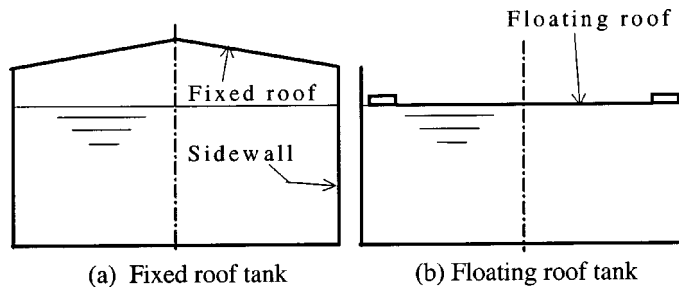


Fig. 1 Oil storage tank roof types

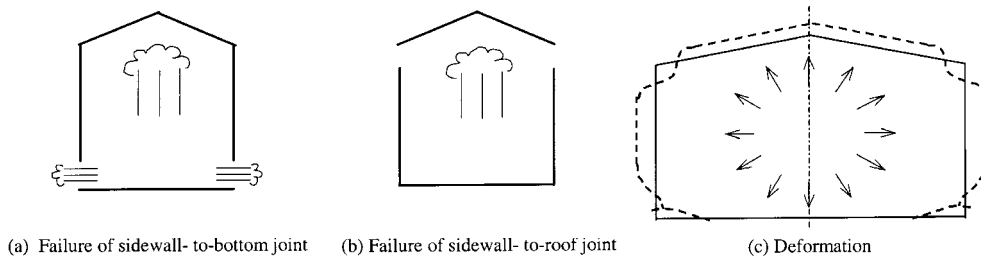


Fig. 2 Deformation and failure types of oil storage tank under internal pressure

circumferential wave number in either joint. The frangible roof joint is designed so that the strength of the sidewall-to-roof joint is weaker than that of the sidewall-to-bottom joint under internal pressure.

This paper presents the bifurcation buckling pressures in both joints under internal pressure. Elastic buckling pressures in the sidewall-to-roof joint and elastic-plastic buckling pressures in the sidewall-to-bottom joint are obtained separately using the axisymmetric finite element method. The effect of roof slope, tank diameter, plate thickness and liquid pressure on the buckling pressure is discussed. The frangible roof joint design can be evaluated for the buckling pressure in the sidewall-to-roof joint to be less than that in the sidewall-to-bottom joint.

## 2. Finite element analysis

The elastic-plastic bifurcation buckling of axisymmetric shells subjected to axisymmetric loads involving large prebuckling deformation has been investigated by many researchers. Bushnell (1976) developed the finite difference computer code BOSOR5, and applied it to various shells. Finite element analyses (FEA) has also been used (e.g., Miyazaki *et al.* 1988). The FEA computer code used in this paper was developed by the author. This analysis consists of prebuckling deformation analysis and bifurcation buckling analysis.

### 2.1 Axisymmetric shell finite element

The axisymmetric shell finite elements used in this study are conical frustum elements, as shown in Fig. 3. The tangential displacement  $u$  and the circumferential displacement  $v$  are assumed to be linear and the normal displacement  $w$  to be cubic with regard to  $s$ , where  $s$  is the meridional

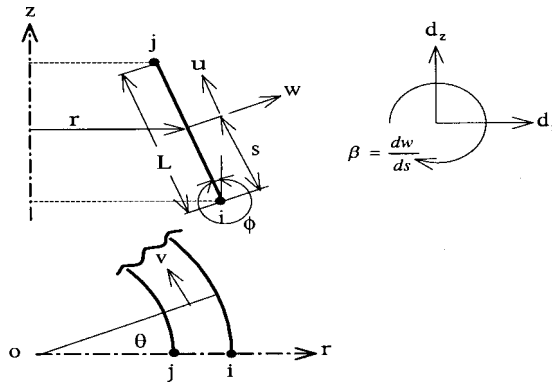


Fig. 3 Axisymmetric shell finite element

coordinate of the shell element. The strain on neutral surface of the shell  $\{e\}$  consists of linear and nonlinear terms, as follows:

$$\{e\} = \{e^{(L)}\} + \{e^{(N)}\} \quad (1)$$

where superscripts  $(L)$  and  $(N)$  denote linear and nonlinear terms. The strain-displacement relation based on the Kirchhoff-Love's assumption is given by the Novozhilov's equation (Stricklin *et al.* 1968) in the following form:

$$\{e^{(L)}\} = \begin{Bmatrix} e_s^{(L)} \\ e_\theta^{(L)} \\ e_{s\theta}^{(L)} \\ \chi_s^{(L)} \\ \chi_\theta^{(L)} \\ \chi_{s\theta}^{(L)} \end{Bmatrix} = \begin{Bmatrix} \frac{\partial u}{\partial s} \\ \frac{1}{r} \frac{\partial v}{\partial \theta} + \frac{1}{r} (w \cos \phi + u \sin \phi) \\ \frac{1}{r} \frac{\partial u}{\partial \theta} + \frac{\partial v}{\partial s} - \frac{v}{r} \sin \phi \\ -\frac{\partial^2 w}{\partial s^2} \\ -\frac{1}{r^2} \frac{\partial^2 w}{\partial \theta^2} + \frac{\cos \phi}{r^2} \frac{\partial v}{\partial \theta} - \frac{\sin \phi}{r} \frac{\partial w}{\partial s} \\ 2 \left( -\frac{1}{r} \frac{\partial^2 w}{\partial s \partial \theta} + \frac{\sin \phi}{r^2} \frac{\partial w}{\partial \theta} + \frac{\cos \phi}{r} \frac{\partial v}{\partial s} - \frac{\sin \phi \cos \phi}{r^2} v \right) \end{Bmatrix} \quad (2)$$

$$\{e^{(N)}\} = \begin{Bmatrix} e_s^{(N)} \\ e_\theta^{(N)} \\ e_{s\theta}^{(N)} \end{Bmatrix} = \begin{Bmatrix} \frac{1}{2} \left( \frac{\partial w}{\partial s} \right)^2 \\ \frac{1}{2} \left( \frac{1}{r} \frac{\partial w}{\partial \theta} - \frac{v}{r} \cos \phi \right)^2 \\ \left( \frac{\partial w}{\partial s} \right) \left( \frac{1}{r} \frac{\partial w}{\partial \theta} - \frac{v}{r} \cos \phi \right) \end{Bmatrix} \quad (3)$$

where  $e_i$  and  $\chi_i(i=s, \theta, s\theta)$  are the strain and the curvature change on the neutral surface of the shell. The strains at a distance  $\bar{z}$  from the neutral surface in shell are defined by the following formula.

$$\{\varepsilon\} = \begin{Bmatrix} \varepsilon_s \\ \varepsilon_\theta \\ \gamma_{s\theta} \end{Bmatrix} = \begin{Bmatrix} e_s - \bar{z}\chi_s \\ e_\theta - \bar{z}\chi_\theta \\ e_{s\theta} - \bar{z}\chi_{s\theta} \end{Bmatrix} \quad (4)$$

The constitutive equation is based on the  $J_2$  flow theory with the isotropic strain hardening rule (Marcal *et al.* 1967), and is written as follows:

$$\Delta\{\sigma\} = ([D^e] + [D^p])\Delta\{\varepsilon\} \quad (5)$$

where  $\Delta\{\sigma\}$  is the stress increment vector,  $\Delta\{\varepsilon\}$  is the strain increment vector, and  $[D^e]$ ,  $[D^p]$  are the stress-strain matrices, which are defined by Eq. (6a) to Eq. (6d), respectively.

$$\Delta\{\sigma\} = [\Delta\sigma_s \quad \Delta\sigma_\theta \quad \Delta\tau_{s\theta}]^T \quad (6a)$$

$$\Delta\{\varepsilon\} = [\Delta\varepsilon_s \quad \Delta\varepsilon_\theta \quad \Delta\gamma_{s\theta}]^T \quad (6b)$$

$$[D^e] = \frac{E}{1-\nu^2} \begin{bmatrix} 1 & \nu & 0 \\ & 1 & 0 \\ \text{sym.} & & \frac{1-\nu}{2} \end{bmatrix} \quad (6c)$$

$$[D^p] = -\frac{1}{S} \begin{bmatrix} S_1^2 & S_1 S_2 & S_1 S_3 \\ & S_2^2 & S_2 S_3 \\ \text{sym.} & & S_3^2 \end{bmatrix} \quad (6d)$$

In Eq. (6a) to Eq. (6d),  $\sigma_i(i=s, \theta)$  is the normal stress component,  $\tau_{s\theta}$  is the shear stress,  $E$  is the Young's modulus and  $\nu$  is the Poisson's ratio. The notation  $\Delta$  denotes the increment.  $S_1$ ,  $S_2$ ,  $S_3$  and  $S$  in Eq. (6d) can be written as follows:

$$S_1 = \frac{E}{1-\nu^2}(\sigma'_s + \nu\sigma'_\theta) \quad (7a)$$

$$S_2 = \frac{E}{1-\nu^2}(\nu\sigma'_s + \sigma'_\theta) \quad (7b)$$

$$S_3 = \frac{E}{1+\nu}\tau_{s\theta} \quad (7c)$$

$$S = \frac{4}{9}\sigma_{eq}^2 H' + S_1\sigma'_s + S_2\sigma'_\theta + 2S_3\tau_{s\theta} \quad (7d)$$

where  $\sigma_{eq}$  and  $H'$  are the von Mises equivalent stress and the strain hardening parameter, and  $\sigma'_i(i=s, \theta)$  is the deviatoric stress component.  $\sigma_{eq}$  is defined by the following formula:

$$\sigma_{eq} = \sqrt{\sigma_s^2 - \sigma_s \sigma_\theta + \sigma_\theta^2 + 3 \tau_{s\theta}^2} \quad (8)$$

In the shell, the membrane forces  $N_s$  and  $N_\theta$ , the shear force  $N_{s\theta}$ , the bending moments  $M_s$  and  $M_\theta$ , and twisting moment  $M_{s\theta}$  are given by the following expressions:

$$N_s = \int_{-t/2}^{t/2} \sigma_s d\bar{z}, \quad N_\theta = \int_{-t/2}^{t/2} \sigma_\theta d\bar{z}, \quad N_{s\theta} = \int_{-t/2}^{t/2} \tau_{s\theta} d\bar{z} \quad (9a)$$

$$M_s = \int_{-t/2}^{t/2} \bar{z} \sigma_s d\bar{z}, \quad M_\theta = \int_{-t/2}^{t/2} \bar{z} \sigma_\theta d\bar{z}, \quad M_{s\theta} = \int_{-t/2}^{t/2} \bar{z} \tau_{s\theta} d\bar{z} \quad (9b)$$

where  $t$  is the shell thickness. The applied loads are handled using the incremental method.

## 2.2. Prebuckling deformation analysis

Prebuckling deformation analysis is equivalent to elastic-plastic large deformation analysis of axisymmetric shells subjected to axisymmetric load. In this analysis, the updated Lagrangian formulation (Bathe *et al.* 1976) is used. It is assumed that the solution obtained at the current step under axisymmetric loading satisfies equilibrium, and that deformation is also axisymmetric in the next step. The displacement vector  $\{d\}$  can be expressed as:

$$\{d\} = \{d_0\} + \Delta\{d_0\} \quad (10)$$

The components of the vector  $\{d_0\}$  are expressed as follows:

$$\{d_0\}^T = [d_{z0} \quad d_{r0} \quad \beta_0] \quad (11)$$

where subscript 0 denotes the axisymmetric deformation, the notations  $d_{z0}$ ,  $d_{r0}$  and  $\beta_0$  are the vertical displacement, the radial displacement and rotational angle, respectively. In axisymmetric deformation, the shear stress and strain are defined to equal zero as follows:

$$\chi_{s\theta} = e_{s\theta} = \varepsilon_{s\theta} = \gamma_{s\theta} = \tau_{s\theta} = N_{s\theta} = M_{s\theta} = 0 \quad (12)$$

According to the virtual work principle, the following stiffness equation is derived:

$$[K_0] \Delta\{d_0\} = ([K_0^{(L)}] + [K_0^{(\sigma)}]) \Delta\{d_0\} = \Delta\{F_0\} + \{R_0\} \quad (13)$$

where  $[K_0]$ ,  $\Delta\{F_0\}$  and  $\{R_0\}$  are the stiffness matrix, the equivalent force increment vector and the residual force vector, respectively.  $[K_0^{(L)}]$  is the small displacement stiffness matrix, and  $[K_0^{(\sigma)}]$  is the initial stress stiffness matrix. All variables in Eq. (13) refer to the current element configurations. In order to derive the elemental stiffness matrix, integration along the meridian is accomplished using the Gauss-Legendre formula with 6 points, and integration through the thickness is accomplished using the Simpson's formula with 20 layers. The nonlinear Eq. (13) is solved using the Newton-Raphson iteration method at each incremental step in this analysis.

To obtain stresses on the yield surface during all plastic deformation, the elastic-predictor radial-return method (Schreyer *et al.* 1979) is used when the beginning-of-step stress at the integral point is elastic or unloading. A trial state based on an elastic assumption is first obtained, and the stress is then corrected with an adjustment in yield surface radius. The solutions of the elastic-plastic problem

based on the  $J_2$  flow theory have to satisfy the following relations:

$$\Delta\{\sigma\}_i = [D^e](\Delta\{\varepsilon\}_i - \Delta\{\varepsilon^p\}_i) \quad (14a)$$

$$\Delta\{\varepsilon^p\}_i = \left\{ \frac{\partial f}{\partial \sigma} \right\}_{i-1} \Delta(\varepsilon_{eq})_i \quad (14b)$$

$$(\sigma_{eq})_i = H((\varepsilon_{eq})_{i-1} + \Delta(\varepsilon_{eq})_i) \quad (14c)$$

$$(\sigma_{eq})_i = f((\sigma_{eq})_{i-1} + \Delta(\sigma_{eq})_i) \quad (14d)$$

where  $f$  is the von Mises yield function,  $\{\varepsilon^p\}$  is the plastic strain vector,  $\varepsilon_{eq}$  is the equivalent plastic strain and  $( )_i$  and  $\{ \}_i$  express the variable or vector at the incremental step  $i$ . Eq. (14a) is the constitutive equation, Eq. (14b) is the normality principle, Eq. (14c) is the material property and Eq. (14d) is the von Mises equivalent stress. If the strain increment  $\Delta\{\varepsilon\}_i$  is assumed to be exact, the solution of the nonlinear simultaneous equations (14a) to (14d) gives the stress increment  $\Delta\{\sigma\}_i$ , the plastic strain increment  $\Delta\{\varepsilon^p\}_i$ , the equivalent stress  $(\sigma_{eq})_i$  and the equivalent plastic strain increment  $\Delta(\varepsilon_{eq})_i$  at the current step  $i$ .

The radial-return method is also used when the stress at the integral point is already plastic. The trial stress  $\{\sigma_t\}_i$  is radially returned to the yield surface as follows:

$$\{\sigma\}_i = \frac{\sigma_{eq}}{\sigma_{eqt}} \{\sigma_t\}_i \quad (15)$$

where  $\sigma_{eqt}$  is the equivalent stress calculated from the trial stress  $\{\sigma_t\}_i$ , and  $\sigma_{eq}$  is that from the equivalent plastic strain  $(\varepsilon_{eq})_i$ .

### 2.3. Bifurcation buckling analysis

Bifurcation buckling analysis follows the prebuckling deformation analysis at each incremental step. The displacement increment at the next step is assumed to have the circumferential wave number  $m$  ( $m \geq 1$ ). The displacement vector can be defined by the following formula to investigate the occurrence of bifurcation buckling.

$$\{d\} = \{d_0\} + \Delta\{d_m\} \begin{pmatrix} \cos m\theta \\ \sin m\theta \end{pmatrix} = \begin{Bmatrix} d_{z0} \\ d_{\theta 0} (= 0) \\ d_{r0} \\ \beta_0 \end{Bmatrix} + \begin{Bmatrix} \Delta d_{zm} \cos m\theta \\ \Delta d_{\theta m} \sin m\theta \\ \Delta d_{rm} \cos m\theta \\ \Delta \beta_m \cos m\theta \end{Bmatrix} \quad (16)$$

The subscript  $m$  denotes the circumferential wave number and  $\theta$  is the circumferential angle. The following stiffness equation is derived from the virtual work principle (Zienkiewicz *et al.* 1988).

$$[K_m] \Delta\{d_m\} = ([K_m^{(L)}] + [K_m^{(\sigma)}]) \Delta\{d_m\} = 0 \quad (17)$$

Throughout the derivation of the stiffness matrix  $[K_m]$ , it is assumed that  $[K_m]$  is independent of the infinitesimal buckling displacements  $\Delta d_{zm} \cos m\theta$ ,  $\Delta d_{\theta m} \sin m\theta$ ,  $\Delta d_{rm} \cos m\theta$  and  $\Delta \beta_m \cos m\theta$ . This

assumption is the so-called “consistent loading”, as defined by Bushnell (1976).

The stability criteria is given by a positive definition of  $[K_m]$ . In other words, if the sign of the determinant of  $[K_m]$  is positive, stability exists. The eigenvector corresponding to the zero eigenvalue becomes the buckling mode.

### 3. Numerical results

#### 3.1. Elastic buckling in the sidewall-to-roof joint

There are two types of fixed roof in oil storage tanks: cone roof tank (CRT) and dome roof tank (DRT), as shown in Figs. 4(a) and (b). The roof slope  $\tan\alpha$  is usually  $1/16\sim 1/6$  in CRT, and the roof radius  $R$  is  $D\sim 1.2D$  in DRT, where  $D$  is the tank diameter. Both the sidewall and roof are welded to the top angle of an L-sectioned beam as shown in Fig. 5. The weight on the roof, such as the roof plate, equipment, and snow, is supported by the roof frame, which is not usually welded to the roof plate because welding stiffens the sidewall-to-roof joint.

Minimum sizes of the sidewall-to-roof joint are stipulated by the Fire Service Law and JIS (Japanese Industrial Standard) B8501 in Japan. According to this law and standard, the minimum

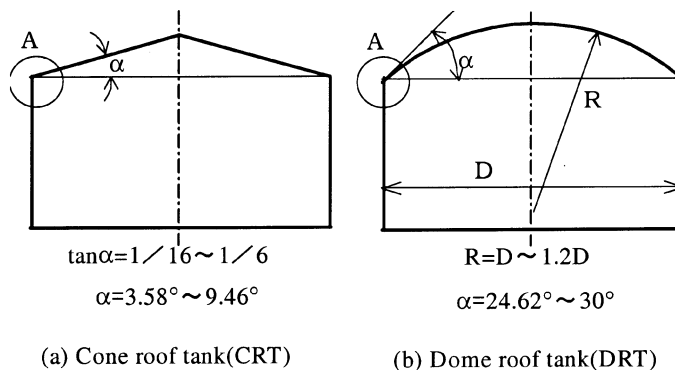


Fig. 4 Types of fixed roof in oil storage tanks

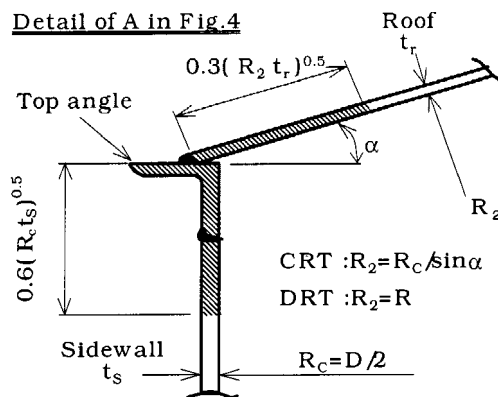


Fig. 5 Compression ring area of sidewall-to-roof joint

Table 1 Minimum sidewall thickness specified by Fire Service Law of Japan

Tank diameter	Sidewall thickness
$D \leq 16$ m	4.5 mm
$16 \text{ m} < D \leq 35$ m	6.0 mm
$35 \text{ m} < D \leq 60$ m	8.0 mm
$60 \text{ m} < D$	10.0 mm

Table 2 Minimum top angle size specified by JIS B8501

Tank diameter	Top angle size
$D \leq 10$ m	L65×65×6
$10 \text{ m} < D \leq 18$ m	L65×65×8
$18 \text{ m} < D \leq 30$ m	L75×75×9
$60 \text{ m} < D$	L90×90×10

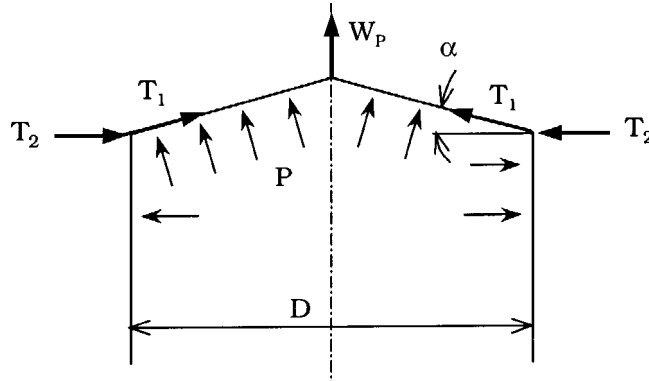


Fig. 6 Equilibrium in the sidewall-to-roof joint under internal pressure

size of both the sidewall and the top angle are given in Table 1 and Table 2 respectively, and the minimum roof plate thickness is 4.5 mm. In existing tanks in Japan, the sidewall-to-roof joint is just these minimum sizes.

According to API Standard 650, Appendix F, the failure pressure of the sidewall-to-roof joint due to internal pressure is derived in the following manner. Fig. 6 shows the equilibrium in the sidewall-to-roof joint under internal pressure. The resultant vertical force  $W_P$  due to the internal pressure  $P$  is given by:

$$W_P = \frac{\pi D^2 P}{4} \quad (18)$$

Equilibrium in the vertical direction at the joint gives the roof force per unit circumference  $T_1$  as follows:

$$T_1 = \frac{W_P}{\sin \alpha \cdot \pi D} = \frac{PD}{4 \sin \alpha} \quad (19)$$

The horizontal component of the roof force can be written as:

$$T_2 = T_1 \cos \alpha = \frac{PD}{4 \tan \alpha} \quad (20)$$

Equilibrium in the radial direction gives the circumferential stress  $\sigma$  of the compression ring:

$$\sigma = \frac{T_2 D}{2A} \quad (21)$$

where  $A$  is the ring area shaded in Fig. 5. Substituting both Eq. (20) and yield stress into Eq. (21),

the failure pressure in the sidewall-to-roof joint is derived in the following form:

$$P_{API} = P(\sigma = \sigma_y) = \frac{8\sigma_y \cdot A \cdot \tan \alpha}{D^2} \quad (22)$$

where  $\sigma_y$  is the yield stress of mild steel and is 220 MPa in API Standard. The above API formula is based on the assumption that failure can be expected to occur when the stress in the compression ring reaches the yield stress. The frangible roof joint design in API Standard should satisfy the following formula.

$$P_{API} \leq P_u \quad (23)$$

The uplifting force  $P_u$  is calculated by:

$$P_u = \frac{4W}{\pi D^2} \quad (24)$$

where  $W$  is the total tank weight excluding the bottom. The API frangible roof joint design is based on static equilibrium, and ensures that yielding of the compression ring will occur before the sidewall-to-bottom joint uplifts in empty tanks.

In the FEA, elastic bifurcation buckling analysis is carried out for internally pressurized sidewall-to-roof joints with the prescribed minimum sizes. The buckling pressure in elastic analysis, that is  $\sigma_y = \infty$ , is larger than that in elastic-plastic analysis. Therefore, the elastic buckling pressure gives a conservative evaluation in the frangible roof joint design. Young's modulus  $E$  is 206 GPa and Poisson's ratio  $\nu$  is 0.3 in the analysis.

The buckling pressure  $P_{cr-u}$  and the corresponding circumferential wave number  $m$  are obtained for various sized tanks using FEA. Fig. 7 shows the relation between the buckling pressure  $P_{cr-u}$  and the tank diameter  $D$ , and Fig. 8 shows the relation between the circumferential wave number  $m$  and  $D$ .  $P_{cr-u}$  decreases rapidly with increasing  $D$ , and  $P_{cr-u}$  in DRT is greater than CRT if the diameter is identical. This means that  $P_{cr-u}$  increases with increasing the roof slope  $\tan \alpha$ . The circumferential wave number  $m$  increases with increasing  $D$  and the variation is nearly linear.

Fig. 9 shows the comparison with the buckling pressure  $P_{cr-u}$  obtained by FEA and the failure pressure  $P_{API}$  by API formula written in Eq. (22), and  $P_{cr-u}$  is greater than  $P_{API}$  for small diameter tanks. It is found that API Standard 650 does not evaluate conservatively in the frangible roof joint

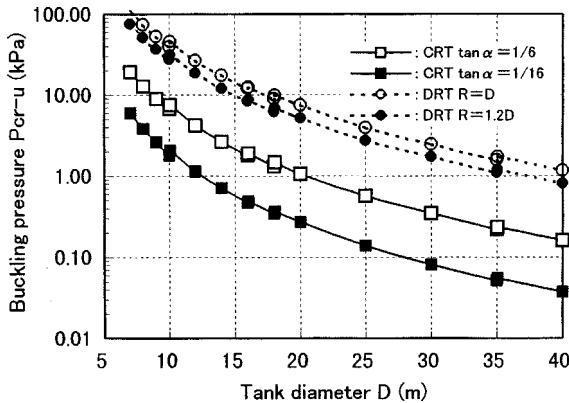


Fig. 7 Elastic buckling pressure in sidewall-to-roof joint

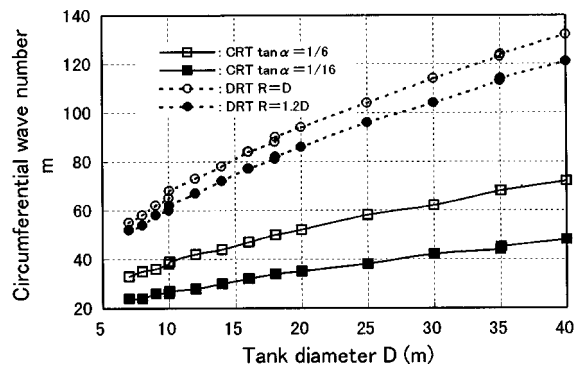


Fig. 8 Circumferential wave number in sidewall-to-roof joint

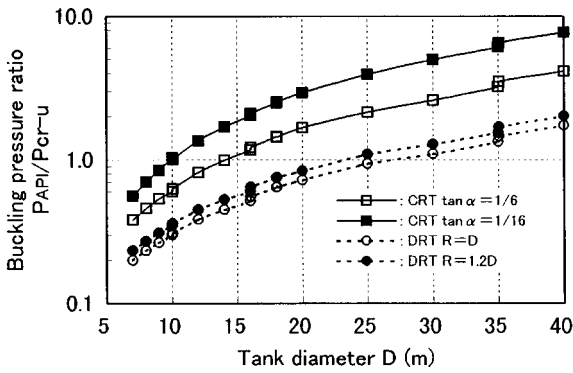


Fig. 9 Buckling pressure ratio in sidewall-to-roof joint

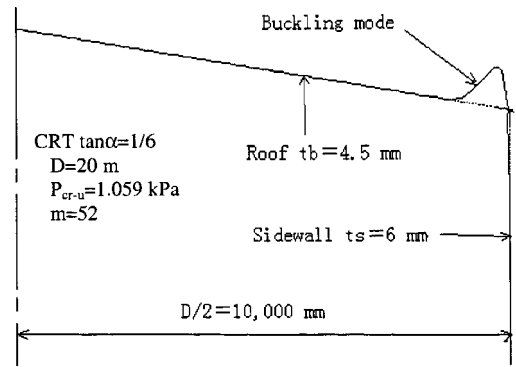


Fig. 10 Buckling mode of sidewall-to-roof joint

design for small diameter tanks. In all cases analyzed here, the buckling modes show local buckling in the roof plate near the joint as shown in Fig. 10.

### 3.2. Elastic-plastic buckling in the sidewall-to-bottom joint

The elastic-plastic buckling in the sidewall-to-bottom joint for small diameter tanks is analyzed. Fig. 11 shows the analytical model. In this figure, the bottom plates rest on a rigid foundation. The liquid pressure with height  $H_L$  and density  $\rho_L$  acts on this joint, and the tank weight  $W$  including sidewall, roof and roof flame is assumed to act at the corner point b. At the beginning of the analysis, the boundary conditions are as follows.

$$a \sim c: d_{z0} = \beta_0 = 0; \quad a: d_{r0} = 0; \quad d: \beta_0$$

The restriction of  $d_{z0} = \beta_0 = 0$  on the bottom will be released when uplifting occurs due to liquid pressure or internal pressure.

The elastic-plastic buckling analysis in the sidewall-to-bottom joint consists of three stages. In the first stage, the analysis is carried out for both the tank weight  $W$  and the bottom plate weight. The second stage is the analysis for liquid pressure, and the third stage is the analysis for internal

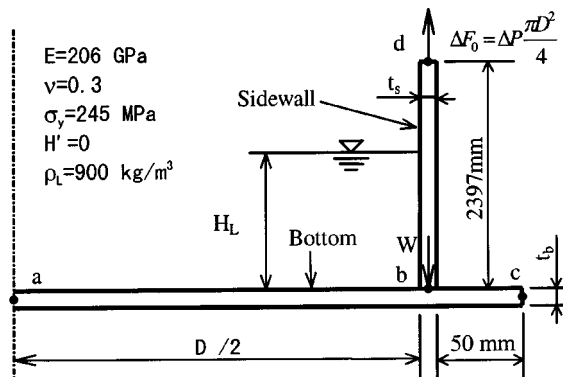


Fig. 11 Sidewall-to-bottom joint model

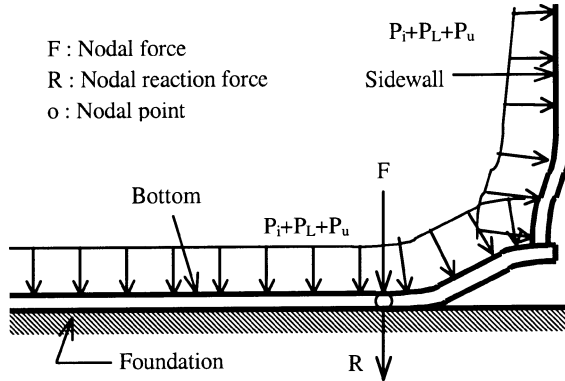


Fig. 12 Uplifted sidewall-to-bottom joint

pressure including the nodal force increment  $\Delta F_0$  at point d shown in Fig. 11. The internal pressure increases until buckling occurs. The buckling pressure  $P_{cr-L}$  for the sidewall-to-bottom joint is defined as follows:

$$P_{cr-L} = P_i + P_u + P_L \quad (25)$$

where  $P_i$  is the internal pressure component of the buckling pressure,  $P_u$  is the uplifting pressure expressed by Eq. (24) and is assumed to be 2.45 kPa in the analysis, and  $P_L$  is the liquid pressure. The sidewall thickness usually varies in the vertical direction in oil storage tanks. The lower sidewall is thicker than the upper.

The uplifting process is shown in Fig. 12 in this analysis. At a nodal point on the bottom, if the equivalent nodal force  $F$  due to internal pressure ( $P_i + P_u + P_L$ ) and bottom weight becomes less than the nodal reaction force  $R$  with an increase in pressure, the displacement restriction at this point can be removed.

Fig. 13 shows the relation between the internal pressure component  $P_i$  of the buckling pressure  $P_{cr-L}$  or the corresponding circumferential wave number  $m$  and the tank diameter  $D$  with the bottom thickness  $t_b=4.5$  mm and the sidewall thickness  $t_s=6$  mm. This figure indicates that  $P_i$  decreases and

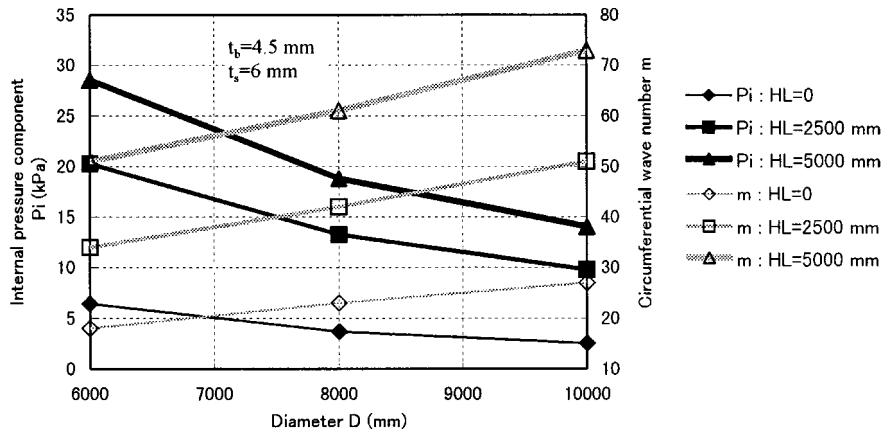


Fig. 13 Internal pressure component of buckling pressure in sidewall-to bottom joint in terms of tank diameter

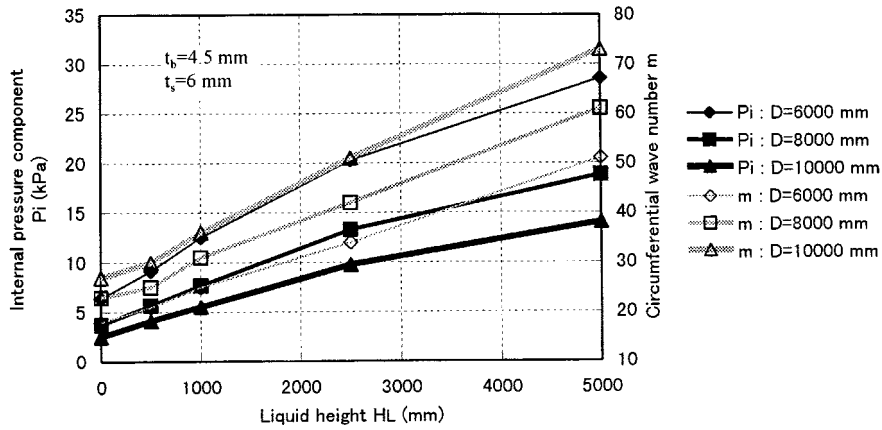


Fig. 14 Internal pressure component of buckling pressure in sidewall-to bottom joint in terms of liquid pressure

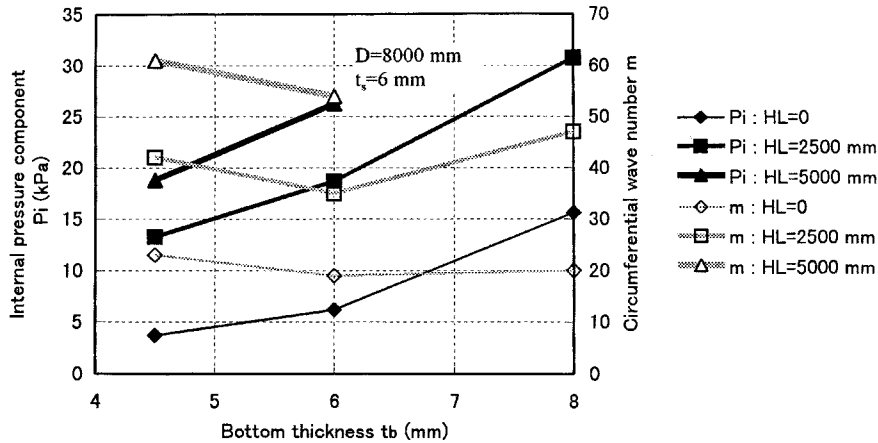


Fig. 15 Internal pressure component of buckling pressure in sidewall-to bottom joint in terms of bottom thickness

$m$  increases with increasing  $D$ , which is similar in tendency to the sidewall-to-roof joint as shown in Fig. 7 and Fig. 8.

Fig. 14 shows the relation between  $P_i$  or  $m$  and the liquid height  $H_L$  with  $t_b = 4.5$  mm and  $t_s = 6$  mm.  $P_i$  and  $m$  increase with increasing  $H_L$ . It can be seen that the liquid pressure  $P_L$  amplifies  $P_{cr-L}$ . Fig. 15 shows the relation between  $P_i$  or  $m$  and  $t_b$  with  $D = 8,000$  mm and  $t_s = 6$  mm. No buckling occurs when  $H_L = 5,000$  mm and  $t_b = 8$  mm. According to Fig. 15,  $P_i$  increases with increasing  $t_b$ , and the effect of  $t_b$  on  $P_i$  is large. Also, an increase in  $t_b$  increases  $m$  in the large  $t_b$  region and decreases  $m$  in the small  $t_b$  region. Fig. 16 shows the relation between the  $P_i$  or  $m$  and  $t_s$  in the case of  $D = 8,000$  mm and  $t_b = 4.5$  mm. According to Fig. 16, an increase in  $t_s$  increases  $P_i$ , but the effect of  $t_s$  on both  $P_i$  and  $m$  is smaller than the effect of other parameters.

The buckling mode is shown in Fig. 17, where  $D = 6,000$  mm,  $H_L = 0$ ,  $t_b = 4.5$  mm and  $t_s = 6.0$  mm. In all cases analyzed here, the buckling modes show local buckling at the bottom near the joint as shown in Fig. 17. Fig. 18 shows the prebuckling deformation at the same conditions as Fig. 17. The

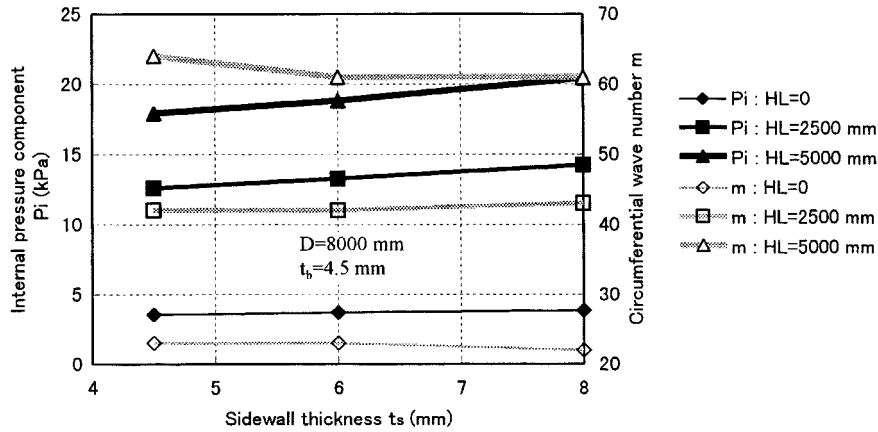


Fig. 16 Internal pressure component of buckling pressure in sidewall-to bottom joint in terms of sidewall thickness

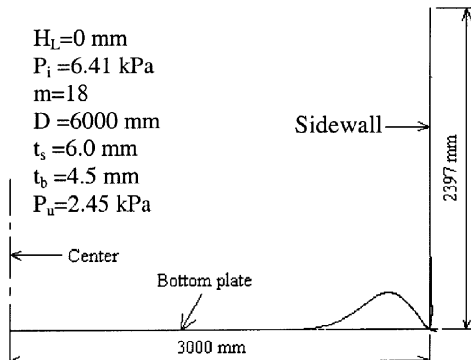


Fig. 17 Buckling mode of sidewall-to-bottom joint

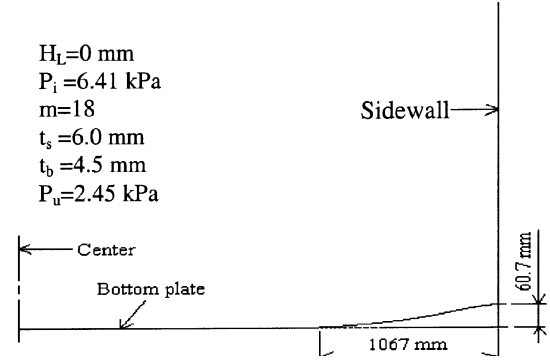


Fig. 18 Prebuckling deformation

uplift displacement at this joint is 60.7 mm and the uplift length at the bottom is 1,067 mm, and the plastic area develops at the bottom near the joint before buckling occurs. Both the uplift displacement and the uplift length of the bottom in liquid-filled tank is smaller than that of the empty tank if the internal pressure ( $P_i+P_u$ ) is identical. The buckling internal pressure  $P_{cr-L}$  is 8.86 kPa in this condition. Assuming that this tank is filled with water to the 10,000 mm level and no internal pressure exist, the pressure on the bottom is 98.07 kPa and the stress of the bottom calculated using the formula proposed by Denham *et al.* (1968) is about 30% of the yield stress. This shows that the sidewall-to-bottom joint can adequately resist the liquid pressure, but is weak against internal pressure.

The buckling pressure  $P_{cr-L}$  with no liquid pressure in the sidewall-to-bottom joint should be greater than the buckling pressure  $P_{cr-U}$  in the sidewall-to-roof joint for a frangible roof joint design.

#### 4. Conclusions

This paper has presented the elastic buckling pressures of the sidewall-to-roof joint and the elastic-plastic buckling pressures of the sidewall-to-bottom joint of aboveground oil storage tanks

under internal pressure. Axisymmetric finite element analysis was carried out. The analysis yielded the following conclusions.

- 1) The failure pressure  $P_{API}$  given by API Standard 650 in the sidewall-to-roof joint is smaller than the elastic buckling pressure  $P_{cr-u}$  obtained by FEA in small diameter tanks.
- 2) API Standard 650 does not evaluate the frangible roof joint design conservatively in small diameter tanks.
- 3) The liquid pressure amplifies the buckling pressure in the sidewall-to-bottom joint.
- 4) The sidewall-to-bottom joint can adequately resist the liquid pressure, but is weak against internal pressure.
- 5) The buckling pressure  $P_{cr-L}$  with no liquid pressure in the sidewall-to-bottom joint should be greater than the buckling pressure  $P_{cr-u}$  in the sidewall-to-roof joint for a frangible roof joint design.

## References

- American Petroleum Institute (1998), "Welded steel tanks for oil storage, Appendix F;" *Design of Tanks for Small Internal Pressures*, API Standard 650, 10th Ed., Washington, DC.
- Bathe K.J., Ramm E. and Wilson E.L. (1975), "Finite element formulations for large deformation dynamic analysis", *International Journal for Numerical Methods in Engineering*, **9**, 353-386.
- Bushnell D. (1976), "BOSOR5-program for buckling of elastic-plastic complex shells of revolution including large deformations and creep", *Computer & Structures*, **6**(3), 221-239.
- Denham, J.B., Russel, J. and Wills, C.M.R. (1968), "A comparison of predicted and measured stresses in a large storage tank", *Proceedings of American Petroleum Institute Refinery Department*, API.
- Lu, Z., Swenson, D.V. and Fenton, D.L. (1996), "Frangible roof joint behavior of cylindrical oil storage tanks designed API 650 Rules", *Journal of Pressure Vessel Technology*, **118**, August, 326-331.
- Marcal, P.V. and King, I.P. (1967), "Elastic-plastic analysis of two-dimensional stress systems by the finite element method", *International Journal of Mechanical Sciences*, **9**, 143-155.
- Miyazaki, N., Hagiwara, S. and Munakata, T. (1988), "Application of the finite element method to elastic-plastic creep buckling analysis of partial spherical shell", *Transactions of the Japan Society of Mechanical Engineers, Series A*, **54**(500), 794-799(in Japanese).
- Morgenegg, E.E. (1978), "Frangible roof tanks", *Proceedings of American Petroleum Institute Refinery Department, 43rd Midyear Meeting*, Toronto, API, 509-514.
- Schreyer, H.L., Kulak R.F. and Kramer J.M. (1979), "Accurate numerical solutions for elastic-plastic models", *Journal of Pressure Vessel Technology*, **101**, August, 226-234.
- Stricklin, J.A., Haisler, W.E., MacDougall, H.R. and Stebbins F.J. (1968), "Nonlinear analysis of shells of revolution by the matrix displacement method", *AIAA Journal*, **6**(12), 2306-2312.
- Zienkiewicz, O.C. and Taylor, R.L. (1988), *The Finite Element Method*, 4th Edition, **2**, McGraw Hill, 284-311.